FISEVIER

Contents lists available at ScienceDirect

Science of the Total Environment

journal homepage: www.elsevier.com/locate/scitotenv



The effect of crystal phase of manganese oxide on the capacitive deionization of simple electrolytes



Su Xu ^{a,b}, TsingHai Wang ^{c,*}, Chu-Fang Wang ^b, Chiu-Wen Chen ^d, Cheng-Di Dong ^d, C.P. Huang ^e

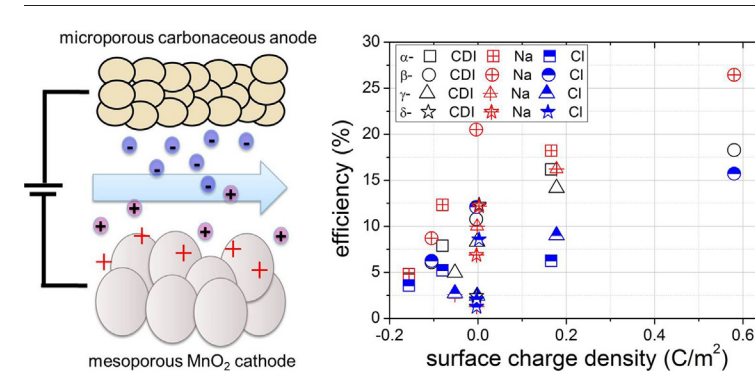
- ^a School of Environmental Sciences and Engineering, Xiamen University of Technology, Xiamen, PR China
- ^b Department of Biomedical Engineering and Environmental Sciences, National Tsing Hua University, Hsinchu, Taiwan
- ^c Department of Chemical Engineering and Materials Science, Yuan Ze University, Zhongli, Taiwan
- d Department of Marine Environmental Engineering, National Kaohsiung University of Science and Technology, Kaohsiung, Taiwan
- ^e Department of Civil & Environmental Engineering, University of Delaware, Newark, DE, USA

HIGHLIGHTS

Capacitive deionization efficiency among different MnO₂ phases was investigated.

- CDI efficiency of studied MnO₂ decreased with increasing negatively surface charge.
- Surface charge effect was likely responsible for different CDI efficiency.

GRAPHICAL ABSTRACT



ARTICLE INFO

Article history: Received 15 January 2019 Accepted 11 April 2019 Available online 16 April 2019

Guest Editor: Hyunook Kim

Keywords:
Capacitive deionization
MnO₂
Surface charge density
Structure induced surface charge effect

ABSTRACT

 MnO_2 is a common material for the fabrication and design of capacitive deionization (CDI) devices but there is little information on the role of MnO_2 crystal phase on CDI performance. A series of MnO_2 (α , β , γ , and δ phase) were synthesized and fabricated as cathodes for studying the CDI performance as affected by pH in simple batch mode experiments. Our results revealed that the deionization efficiency decreased with increased negative surface charge as a result of the deprotonated surface. Importantly, this correlation was pH independent and the surface heterogeneity due to different MnO_2 phase was likely responsible for the different degree of surface ionization and consequently the CDI efficiency. Results of electrochemical impedance spectroscopy analyses further implicated that a highly ionized surface would result in a diffusion layer with a great resistance that conversely inhibited the access of co-ions in the CDI process. This indicated the applied potential was mainly responsible for driving ions transporting through the double layer resistance instead of accommodating them (electrosorption). Based on our results, the surface heterogeneity as a result of different spatially distributed MnO_6 octahedral would be accounted for the varying degree of surface ionization and consequently the discrepancy in CDI efficiency among different MnO_2 phases.

© 2019 Elsevier B.V. All rights reserved.

* Corresponding author. E-mail address: thwang@saturn.yzu.edu.tw (T. Wang).

1. Introduction

Rapid population growth and increase in extreme weather events have impacted the supply of fresh water sources and thus prompted the industries to desalinate seawater and brackish water (Liu et al., 2017). Conventional desalination technologies such as thermal distillation evaporation (Shahzad et al., 2017), reverse osmosis (Ray et al., 2017), and electrodialysis (Abou-Shady, 2017), though commercially available, consume intensive energy (Xu et al., 2017). The awareness in the balance between energy efficiency, water treatment efficiency and environmental impacts are thus emerging in the environmental engineering community (Pan et al., 2018). Capacitive deionization (CDI) has evolved for removing salt or ionic impurities from aqueous solutions as an alternative (Wang et al., 2017a). Compared to other conventional technologies, CDI has several advantages including low operation voltage, high salt removal capability, low chemical demand, and no secondary wastes (Ahualli et al., 2017; Linnartz et al., 2017).

Capacitive deionization is an electrochemical desalination process taking place at the electrical double layers (EDL) developed at the electrode surface (Suss et al., 2015). Murphy and Caudle were among the early researchers to study ion removal in flow-by cell using carbonaceous electrodes (Murphy et al., 1965). By applying an external bias, an electrostatic field across the electrodes forms electrical double layer adjacent to the electrode that is capable of retaining ions at the solution-electrode interface (Liu et al., 2016a). Upon termination of the external bias, the absorbed ions are readily released into the bulk solution (Prehal et al., 2017). The most frequently employed electrode materials in CDI cells are carbonaceous materials including carbon aerogels (Macias et al., 2017), mesoporous carbon (Wang et al., 2017b), and carbon black derivatives (Liu et al., 2016a; Xu et al., 2016). Recently, the combination of redox-sensitive transition metal oxides with carbonaceous materials significantly improves the electrochemical property and current efficiency in ion separation (Choi et al., 2017). Among various transition metal oxides, manganese dioxide (MnO₂), with several advantages including low cost, high abundance, environmental friendly, has been widely used in electrochemical applications such as supercapacitors (Shao et al., 2016). MnO₂/carbon composite electrode is known to greatly enhance the specific capacitance of supercapacitors (Huang et al., 2017) and CDI cells through the combination of Faradaic reaction and electrical double-layer charging (Yang et al., 2011; El-Deen et al., 2014).

Various MnO₂(s) crystal phases have been used to make CDI cells with great improvement in ion separation performance. Zou et al. have demonstrated that the NaCl adsorption capacity of α -MnO₂/ nanoporous carbon composite electrode is about 3 times (16.9 µmol-Na/g) greater than that of a commercially available activated carbon electrode (5.4 µmol-Na/g) operated at 2 V (Yang et al., 2011). The authors have attributed the higher salt removal capacity to the higher capacitance of α -MnO₂/nanoporous carbon composite electrode. Chen et al. have reported that the desalination capacity of δ -MnO₂/MWCNTs (multi-walled carbon nanotubes) is about four times (6.65 mg-Na/g) higher than that of virgin MnO₂ electrode (1.60 mg-Na/g). Enhanced salt removal is attributed to the increase in surface area of the carbonaceous support (Chen et al., 2016). Liu et al. have reported a superior electrosorption capacity that is 1.6-fold (9.3 mg-Na/g) greater than that of pure carbon electrode (5.7 mg-Na/g) using an amorphous-MnO₂/activated carbon composite electrode (Liu et al., 2016b). They further suggested that the mixed capacitive-Faradaic process, corresponding to the combination of the double-layer charging and the pseudocapacitive redox reaction of MnO₂, is responsible for the significant improvement in desalination performance (Liu et al., 2016b). El-Deen et al. have used a graphene wrapped with α -MnO₂(s) and observed electrosorptive capacity higher than that of MnO₂-nanorods@ graphene electrode and attributed the improvement in desalination to the morphology of $MnO_2(s)$ (El-Deen et al., 2014).

In summary, it is clear that incorporating MnO₂(s) with carbonbased materials can effectively improve ion separation efficiency in CDI applications, however, there is little information on the effect of MnO₂(s) crystal phase on the performance of CDI process (Li et al., 2015). We hypothesize that the crystal structure of $MnO_2(s)$ plays a key role in CDI capacity. In order to verify the above hypothesis, a series of MnO₂ phases (α -, β -, γ - and δ - MnO₂) were synthesized and used as CDI electrodes. The electrodes were characterized for morphology (by scanning electron microscopy, SEM), crystal structure (by X-ray diffraction, XRD), specific surface area (by N₂ adsorption according to the Brunauer-Emmertt-Teller, BET, equation), and surface acidity (by alkalimetric titration and zeta-potential measurements). The capacitive behavior was assessed with electrochemical impedance spectroscopy (EIS). Batch mode CDI experiments were conducted to determine the desalination efficiency (in terms of conductivity change). Results were used to describe the effect of MnO₂ phase and related surface charge effect on the distribution of surface charge density over MnO₂ surfaces on CDI performance.

2. Materials and methods

2.1. Synthesis of MnO₂

All chemicals used in this study were purchased from Sigma-Aldrich and used as received. α-MnO₂ was synthesized by dissolving 4.06 g (26.8 mmol) of MnSO₄ and 3.79 g (23.9 mmol) of KMnO₄ in 60 mL DI water, then the mixture was heated at 100 °C under continuous reflux for 20 h with vigorous stirring (Yang et al., 2011). The as-synthesized product was filtered, washed with DI water, and dried at 85 °C overnight. β- MnO₂ was synthesized by adding 1.6 mmol of MnSO₄ and 1.6 mmol of Na₂S₂O₈ into 20 mL DI water at room temperature. The mixed solution was loaded in a Teflon-lined autoclave for hydrothermal reaction at 120 °C 12 h (Li et al., 2015). Then, the autoclave was cooled and products were washed with DI water and dried at 85 °C overnight. γ -MnO₂ was synthesized by dissolving 16 mmol of MnSO₄ and 16 mmol of Na₂S₂O₈ in 200 mL of DI water, then the mixed solution was heated under stirred with continuous reflux at 90 °C for 24 h (Li et al., 2015). The precipitate was filtered, washed with DI water and dried at 85 °C overnight. δ-MnO₂ was synthesized by dissolving 0.38 M of KMnO₄ in 50 mL of DI water. The solution was mixed with 1.4 M of glucose in 20 mL DI water (Chen et al., 2016). The brownish gel was then dried at 85 °C for 24 h followed by calcination at 450 °C for 2 h. The resulting powder was washed with DI water and dried at 85 °C overnight.

2.2. Characterization of $MnO_2(s)$

The surface morphology of all MnO₂(s) samples was examined using scanning electron microscope (SEM, JSM700F, JEOL). X-ray powder diffraction (XRD) analysis was performed with D2 Phaser diffractometer (Bruker, Germany) using Cu K α radiation ($\lambda = 1.5418 \text{ Å}$) at a scan rate of $1^{\circ}(2\theta)$ /min and scan range from 10° to 80° . The specific surface area (S_{BET}) was measured using a N₂-physisorption analyzer (Micromeritics ASAP 2020). Alkalimetric-acidimetric titration was conducted to characterize the surface acidity of MnO₂. MnO₂ was dispersed in solutions at ionic strength of 10 and 1.0 mM NaCl and solid/liquid ratio of 10 g/L. The mixture was let stand for one week to allow full hydration and development of surface hydroxyo groups. After equilibrium for one week, the mixture was bubbled with N2 gas for 30 min to remove dissolved CO₂ and then titrated with 0.1 M HCl/NaOH. The pH was recorded at 2 min after the addition of an aliquot of titrant. The surface charge/surface charge density, Q, was calculated by the following equation (Stumm and Morgan, 1995; Huang and Stumm, 1973):

$$(C_b - C_a + [H^+] - [OH^-])/\mathbf{a} = \{ \equiv MnOH_2^+ \} - \{ \equiv MnO^- \} = Q$$
 (1)

$$\sigma_0 = Q \times F/s \tag{2}$$

where {} indicates the concentration of ionized MnO₂(s) surface species (defined as the \equiv MnOH species, mol/g), [H⁺] and [OH⁻] are derived from the recorded pH, C_b and C_a are concentration (mol/L) of strong base/strong acid added, **a** is the quantity of oxide (g), Q is the mean surface charge (mol/g), s is the specific surface area (m²/g); σ_0 is the surface charge density (C/m²) and F is Faraday constant (96,500 C/mol).

2.3. CDI experiments

To assess the effect of MnO_2 phase on CDI performance, the electrodes were fabricated by following steps (Fan et al., 2016). The titanium substrates (1 cm \times 1 cm) was acid activated by heating in 6.0 M HCl solution at 80 °C for 2 h. The activated Ti substrates were then washed with ethanol and DI water and dried at 85 °C 24 h. The MnO_2 /carbon black (CB) paste was prepared by mixing as-synthesized MnO_2 (s) (4.5 g of different phase) with CB (0.5 g). Polyvinylidene difluoride (PVDF, MV = 534,000, 0.4 g) and N-Methyl-2-pyrrolidone (NMP, 8 mL) were used as the binder and organic solvent, respectively. The mixture of MnO_2 /CB paste as well as polymeric binder and organic solvent was agitated for 24 h and then spread over the activated titanium substrate using a blade. The electrode was left at 80 °C for 12 h to evaporate all organic solvents remaining in the electrode pores.

In order to determine the CDI efficiency, batch-mode experiment was conducted in a borosilicate glass beaker containing 50 mL of 1.0 mM NaCl solution. The CDI cell was composed of a MnO₂ working electrode (cathode) and a carbon counter electrode (the anode without MnO₂) separated by 2 mm using transparent tape (3 M tape) as spacers (Scheme 1). As our cathode was mainly composed of MnO₂ whose conductivity was much lower than the carbonaceous anode (Scheme 1), our experiments were conducted at -1.8 V (cathode) although a window of 0.8 to 1.2 V is usually adopted (Gao et al., 2015; Lado et al., 2013; Gao et al., 2016). Three testing cells were utilized in each test (total effective surface area of 3 cm²) and the CDI testing was conducted in triplicate (9 CDI cells of each MnO₂ phase were used). The conductivity and the concentration of Na⁺ and Cl⁻ ions were recorded using a portable conductivity meter (HQ40d, Hach), ICP-MS (Agilent 7500A), and chloride selective electrode (Metrohm), respectively. The deionization efficiency, η , was defined by change of conductivity during the charging process:

 $\eta = (C_0\!-\!C_f)/C_0 \times 100\%$

where C_0 and $C_{\rm f}$ are the initial and final conductivity of the NaCl solution.

2.4. Electrochemical measurement

The electrochemical characteristics of MnO2 electrode were examined by electrochemical impedance spectroscopy (EIS). All experiments were recorded using a CHI electrochemical station (CHI 608E, CH Instrument) with MnO₂ electrode as a working electrode and carbon electrode as a counter electrode in 1.0 mM NaCl solution. For EIS measurement, either -0.001 V or -0.7 V bias were applied in the frequency ranging from 1 Hz to 0.1 MHz and obtained EIS spectra were fitted trial-and-error with an equivalent circuit using the Zview software (Scribner Associates Inc.). To minimize deviations propagating from the fitting processes, the following protocol was followed based on several approximations and considerations (Liu et al., 2017; Wang et al., 2016). First, a 2-component equivalent circuit was adopted. This arrangement was to avoid introducing additional variables that were not supported by any physical meanings although it is certain that the more variables introduced, the more precise fittings can be achieved. In this configuration, we assigned the first component the Stern layer and the second component the diffusion layer of the electrical double layer. In this configuration, charge transport usually occurs in the high frequency region while the motion of ions is often observed in the low frequency region due to their much heavier mass (in comparison with charges such as electrons). As both charge transport and ion movement were expected to occur at the solid/solution interface and the diffusion layer (additional electric field generated by either surface charge or applied bias), the simple 2-component model was sufficient to minimize the variation propagation resulting from those non-defined variables. Once the associated physical background of adopted equivalent circuit was defined, the fitting started with determining the second component (low frequency region) by giving fixed values for the first component, i.e., the intercept of the first semicircle was assigned the resistance (R_1) of the first component. We then fixed the as-obtained R₂ and C₂ and left the R₁ and C₁ to be fitted by the Zview software. In the last step, all four variables were set free for fitting and the best fitting with the smallest Chi-squared value was hence determined. This procedure is very important as it avoids producing unreal values, i.e., a unreal resistance ($> 100 \text{M}\Omega$).





Scheme 1. Illustration of the CDI experiment setup conducted in this study.

3. Results and discussion

3.1. Surface morphology and structure characterization

Although all MnO₂ phases have the same Mn(IV) oxidation state, they essentially have different spatially distributed manganese oxide octahedral (MnO₆) being incorporated into the MnO₂ unit cell, e.g., α- MnO_2 (2 × 2), β - MnO_2 (1 × 1), γ - MnO_2 (1 × 1 or 1 × 2) and layered δ- MnO₂. This arrangement results in the uneven distributed electron density (cloud) in the MnO₂ lattice and at the MnO₂ surface and consequently different surface chemical behaviors of different MnO₂ phases. In fact, this assumption is exactly the basis of first-principles calculations to investigate the surface chemistry of different phases and facets of TiO₂ (Albert et al., 2018; Fazio et al., 2018) and MnO₂ (Chen et al., 2017; Yang et al., 2018). In other words, unevenly distributed electron density at the surface of material results in the existence of surface permanent charge (fix charge) and by this manner influences its surface chemical behaviors. As little redox reactions are involved in the CDI process (CDI process is a capacitive adsorption, not a redox reaction such as water electrolysis) (Xu et al., 2016; Choi et al., 2017), we thus speculate that the CDI efficiency should be mainly affected by the surface chemistry of these MnO₂. Taking this into consideration, we probably might find a universal answer accounting for how the surface chemistry of MnO₂ itself influences the afterward CDI efficiency. Fig. 1 shows the SEM images and corresponding XRD patterns of as-synthesized MnO₂ samples. All synthesized MnO₂ samples were well indexed by corresponding diffraction patterns (α-MnO₂ (JCPDS 44–0141), β-MnO₂ (JCPDS 24–0735) and γ -MnO₂ (JCPDS 14–0644) and δ -MnO₂ (JCPDS 52–0556)), indicating the success all MnO₂(s) synthesis. The appearance of $MnO_2(s)$ samples is also different: α - $MnO_2(s)$ is consisted of nanowires; β -MnO₂(s) has a nanorod morphology; γ -MnO₂ (s) exhibits an appearance of nanoflower composed of stacked rods; and δ -MnO₂(s) contains small nanospheres and nanoplates. Importantly, none of the synthesized MnO₂(s) has significant porous appearance as indicated by SEM images. This explains the low surface areas of these samples as suggested by BET analyses (Table 1). Although it is often expected that high surface area would lead to enhanced adsorption capability (Chen et al., 2016), our results clearly indicates that β -MnO₂(s) has the lowest specific surface area (Table 1) yet exhibits the highest CDI efficiency (Fig. 2a).

3.2. CDI performance

In order to explore the effect of MnO₂ phase on CDI performance, batch mode tests were conducted in triplicate and the CDI efficiency was presented in Fig. 2a. Results showed that the β-MnO₂ (s) electrode exhibited the highest CDI efficiency over other electrodes while the CDI efficiency of δ -MnO₂ electrode was the lowest. Huang has reported that the crystal field profoundly influenced the compacted layer capacity, C_{comp}, of metal oxides, in which the amorphous metal oxides generally had lower C_{comp} than the well crystalline counterparts (Huang, 1976). While the CDI efficiencies decreased with increasing pH in all electrodes, the zeta potential became much negative along with increasing pH too (Fig. 2b). Generally, the CDI efficiency is observed increased with increasing zeta potential (Choi et al., 2017; Shao et al., 2016). This means the δ -MnO₂ electrode should exhibit the highest CDI efficiency over others as it possesses the most negative zeta potential. Apparently, zeta potential alone is insufficient to fully account for the surface charge effect on CDI efficiency among different MnO₂ phase electrodes.

In order to gain better insight into the surface chemistry of different MnO_2 phases, alkalimetric-acidimetric titration of MnO_2 suspensions in two different ionic strengths was conducted (Fig. 3a–d). The surface charge density of MnO_2 (C/m^2) resulting from the ionization of surface

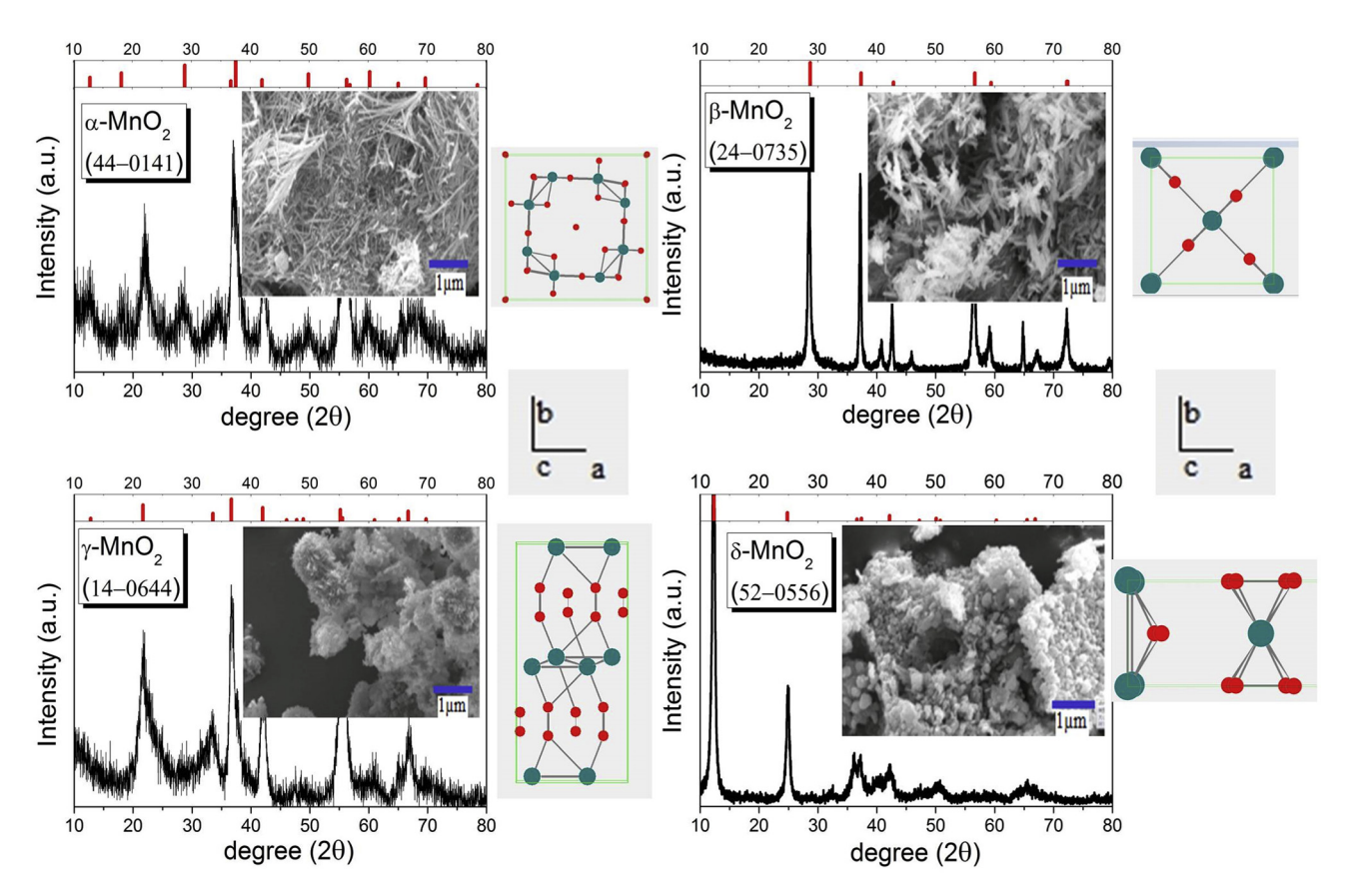


Fig. 1. Representative SEM images and XRD patterns of as-synthesized different phase MnO₂. Inserted lattice structures were produced using PowderCell version 2.4 software where the red and green spheres stand for the Mn and O atom, respectively.

Table 1Surface area and porous properties of as-synthesized MnO₂ samples determined by BET analyses.

S	amples	Surface area S _{BET} (m ² /g)	Pore size d [nm]	Pore volume V (cm³/g)	Micropore volume V _{micro} (cm ³ /g)
α	-MnO ₂	47.2	31.2	0.36	8.7×10^{-3}
β	$-MnO_2$	13.6	22.3	0.07	8.5×10^{-4}
γ	-MnO ₂	43.3	9.0	0.07	2.2×10^{-3}
δ	$-MnO_2$	97.5	51.3	0.57	7.0×10^{-3}

hydroxyl groups (≡MnOH) was thus determined (Huang and Stumm, 1973; Stumm and Morgan, 1995). Note that the negative sign in surface charge density is assigned to the deprotonation of surface hydroxyl groups herein. It is noted that the surface charge density curves of γ - $MnO_2(s)$ (Fig. 3c) and δ - $MnO_2(s)$ (Fig. 3d) in two different ionic strengths were highly superimposed, indicating that surface ionization of both phases was unaffected by the ionic strength. Interestingly, they both were the phases that exhibited the lowest CDI efficiency. By contrast, the surface charge density curves of α -MnO₂(s) (Fig. 3a) and β -MnO₂(s) (Fig. 3b) in two ionic strengths were not superimposed. This means that ionic strength would shift the degree of surface ionization (and therefore the point of zero charge, pH_{zpc}). If all surface hydroxyl groups (=MnOH) were identical and their ionizations were unaffected by neighboring hydroxyl groups (assuming a homogeneous surface), then the titration curve should be independent of the ionic strength (Huang and Stumm, 1973; Stumm and Morgan, 1995). Apparently, the surface of α -MnO₂(s) and β -MnO₂(s) were relatively heterogeneous in comparison with that of γ -MnO₂(s) and δ -MnO₂(s). In this case, each loss of a proton reduces the charge on the polyacid and thus affects the acidity of the neighboring groups (Huang and Stumm, 1973). Accordingly, shifted pH_{zpc} in $\alpha\text{-MnO}_2(s)$ (Fig. 3a) and in $\beta\text{-MnO}_2$ (s) induced by the ionic strength effect was observed (Fig. 3b). Based on above observations, it is speculated that surface heterogeneity among different MnO₂(s) phases is likely responsible for the degree of surface ionization and hence the CDI efficiency.

To further explore the dependency between deionization efficiency and surface ionization, deionization efficiencies in the pH range of 4 and 10 were expressed as a function of surface charge density (Fig. 3e). The deionization efficiency at pH 3 was excluded as at this pH the ionic strength has been altered by the pH adjustment. An interesting pattern appeared in Fig. 3e when plotting the CDI efficiency against surface charge density. Obviously, ionization of surface hydroxyl groups significantly influences the CDI efficiency among different MnO₂ phases in addition to their surface potential (as measured by zeta potential). A general pattern was that regardless of the crystal phase of MnO₂, high CDI efficiency was always related to high degree of protonated

surface hydroxyl groups (highly positive surface charge density) in a given MnO₂ phase.

Note that theoretically the surface charge density determined by titration is not always equal to the surface charge density recorded by zeta potential measurement. This is because the former is simply as a result of surface ionization while the latter would be the combination of surface charge resulting from the surface ionization and the fix charge originated from uneven distributed electron density. For instance, the highly negative zeta potential in δ -MnO₂ (Fig. 2b) is likely as a result of its unique layered structure. This speculation is based on the recent molecular dynamics simulations, which suggested that there are three distinct surface sites at layer-structured muscovite actively responsible for Na⁺ ions adsorption. Identified surface sites included a Si₄Al₂ ditrigonal cavity site, an Al site, and a site that allow accommodation of hydrated Na cations (Kobayashi et al., 2017). While the latter two sites are essentially attributed to surface hydroxyl groups that exist in all MnO₂ phases, the unique ditrigonal cavity site resulting from the successive MnO₆ octahedral network of δ -MnO₂ is likely accounting for its much negative zeta potential over other phases (Fig. 2b). This means that unlike other 3D structured MnO₂ phases (α -, β -, and γ -MnO₂), the surface charge of δ-MnO₂ is mainly resulted from its layered structure (fixed charged as a result of uneven distributed electron density) instead of the ionization of surface hydroxyl groups.

Aside from the intrinsic difference in the 2D/3D configuration, question remains on how the structure effect influences the ionization of surface hydroxyl groups and consequently the CDI efficiency among α -, β -, and γ -MnO₂ phases. A likely explanation would be that the surface potential arising from the ionized surface hydroxyl groups would concurrently decrease Cl⁻ adsorption (co-ion exclusion effect) (Gao et al., 2015; Lado et al., 2013; Gao et al., 2016). As shown in Fig. 3e, adsorption of Na⁺ (red dataset) was unaffected by the positive surface charge, some of their removal efficiency were even higher than the changes in conductivity (black dataset). This is likely a result of applied negative potential in CDI process (cathode). On the contrary, the removal efficiency of Cl- (blue dataset) was obviously much lower than that of Na+ and conductivity in the same condition. As the conductivity of a solution can be expressed as the sum of all individual ions (both cation and anion) of the electrolyte (the Kohlrausch's law), reduced (electro)adsorption of Cl⁻ as a result of ionized surface hydroxyl groups consequently decreased the CDI efficiency. On the other hand, the relative heterogeneous surface of α -MnO₂(s) and β -MnO₂(s) influenced the degree of surface ionization and therefore the structural ordering of the water layer immediately adjacent to the solid surface (Huang and Stumm, 1973). This allowed α -MnO₂(s) and β -MnO₂(s) have high Cl⁻ (electro)adsorption affinity and therefore high CDI efficiency.

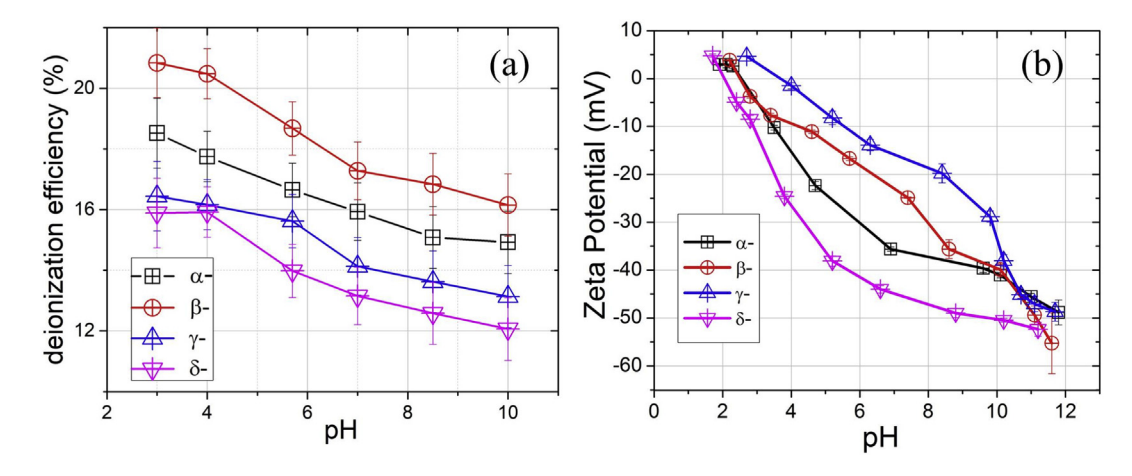


Fig. 2. (a) CDI efficiencies and (b) zeta potentials as a function of pH of different MnO₂ electrodes.

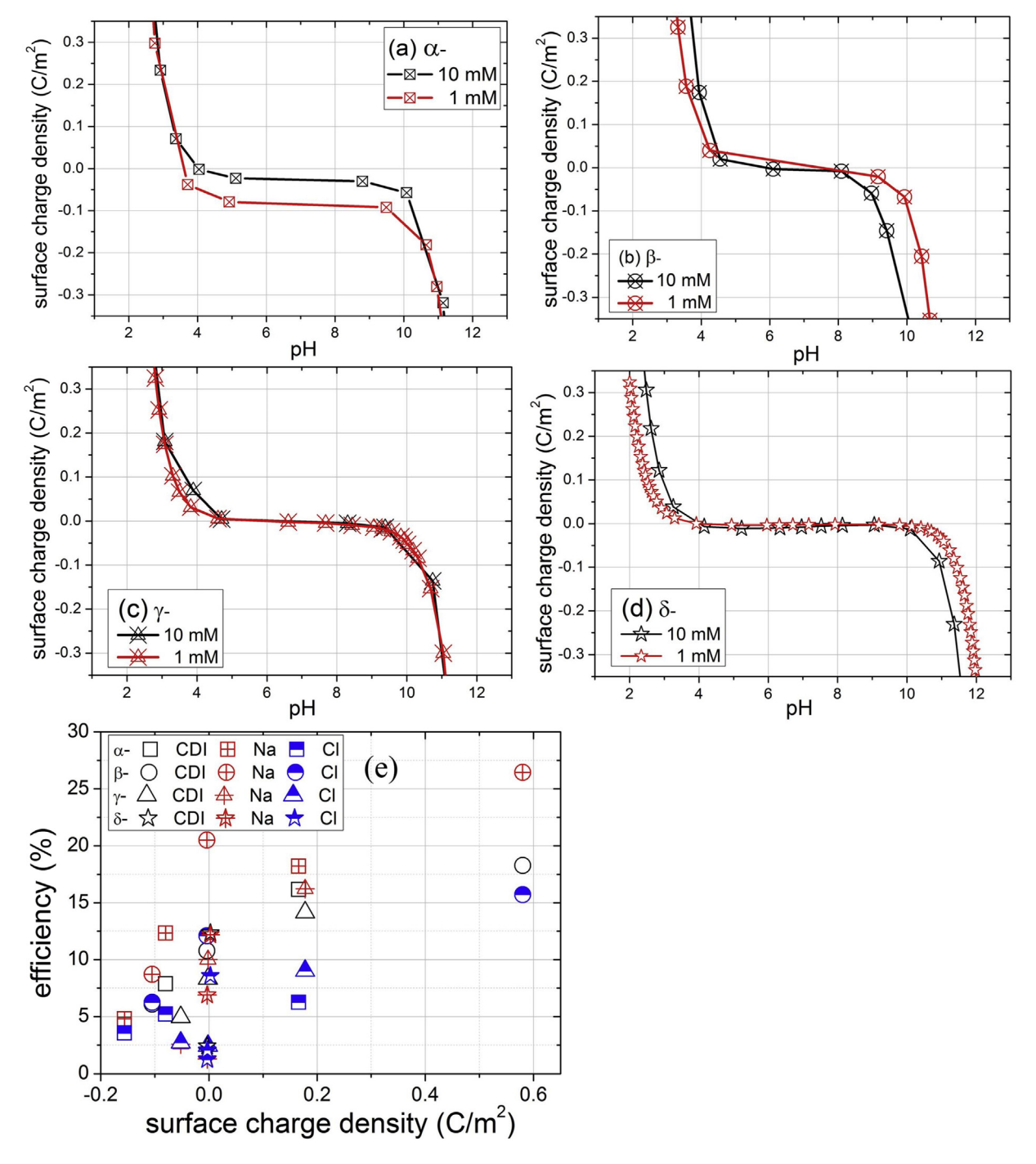


Fig. 3. As-determined surface charge density as a function of pH of (a) α —, (b) β —, (c) γ —, and (d) δ —MnO₂ in 10 mM (filled) and 1.0 mM (open) NaCl solutions and (e) the dependency of deionization efficiency as well as Na⁺/Cl⁻ removal ratio and surface charge density among different MnO₂ phases.

3.3. EIS analyses

In order to explore the electrochemical behavior of different MnO_2 phases in CDI process, additional EIS measurements were conducted with $\beta\text{-MnO}_2(s)$ and $\delta\text{-MnO}_2(s)$ electrodes (as they possessed the highest/lowest CDI efficiency among all electrodes). The frequency dependence of the impedance of the carbon (as a reference), $\beta\text{-MnO}_2(s)$ and $\delta\text{-MnO}_2(s)$ electrodes collected in the working solution (1.0 mM NaCl, pH = 7) is shown in Fig. 4. For the control electrode, three impedance regions (Hz < 10^2 Hz, 10^2 Hz - 10^4 Hz, and > 10^4 Hz, respectively) w/o applying bias were noted. Interestingly, the difference between the first two regions was not significant and they both were

independent to the increasing frequency. The third impedance region, however, decreased significantly with increasing frequency. Given the movement of ions and electrons would be observed at low and high frequency region, respectively (Li et al., 2018; Wang et al., 2014), reduced impedance at high frequency region is simply reflecting the conductive nature of carbon black. On the other hand, the observed impedance at the two low frequency regions presumably suggested that ions could transport readily in the tortuous paths in the carbonaceous electrode without experiencing any significant dragging force. Importantly, impedance of carbon electrode was unaffected by the applied bias, meaning again the conductive nature of the carbonaceous electrodes.

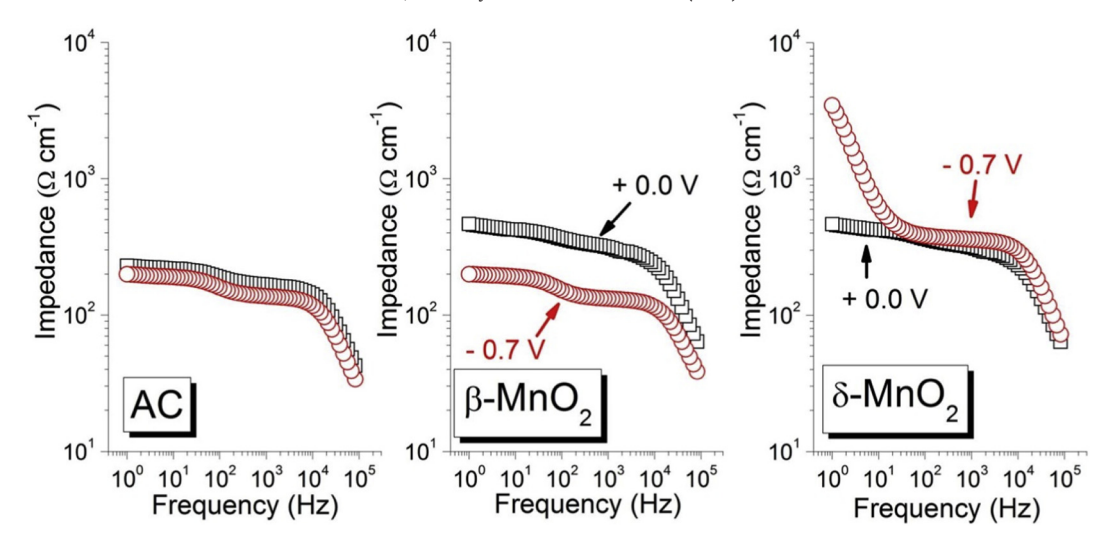


Fig. 4. Impedance dependency as a function of frequency of control (carbon), β -MnO₂ and δ -MnO₂ electrodes.

In β–MnO₂ electrode, introducing active MnO₂ slightly increased the impedance of the electrodes, likely arising from the boundary resistance at MnO₂ and carbon interfaces. However, the impedance dropped significantly to a level comparable to that of carbon electrode when bias was applied. This indicated that boundary resistance at MnO₂ and carbon interfaces was not significant. Similarly, the impedance of the δ -MnO₂ electrode without applying bias was rather comparable to that of β-MnO₂ electrode in the same condition. When charging, the impedance of the δ-MnO₂ electrode at low frequency region however increased significantly. This suggested that ion transporting at δ-MnO₂ electrode would experience an additional dragging force. To quantitatively interpret this interface behavior, collected EIS spectra were further fitted with a 2-component equivalent circuit where the first and the second component represented the electrical behavior occurring at the electrode/electrolyte interface and the diffusion layer, respectively (Fig. 5). This arrangement was to avoid introducing additional variables that are not fully supported by any physical meanings although it is certain that the more variables introduced, the more precise fittings can be achieved. This assignment was also based on the observation shown in Fig. 5 where there were only two significant semicircles noted in the Nyquist plot. As shown in Fig. 5a, the complex plane data contains low frequency data on the right side of the plot and those collected at higher frequencies are on the left. The Nyquist plot of the control electrode (carbon electrode) exhibited two semicircles, each of which was representative of association with a single time constant element due to charge transfer phenomenon across the frequencies. Fitting results quantitatively revealed that the charging slightly decreased the resistance at the solid-electrolyte interface but had limited influence on the resistance and capacitance at the solid-electrolyte interface and the diffusion layer (within the experimental standard deviation). In the case of β -MnO₂(s) electrode, slightly increased resistance and dramatic decreased capacitance by almost three orders of magnitude were noted when no bias was applied. On the contrary when bias was applied, determined resistance and capacitance at the diffusion layer became rather comparable to that of the carbon electrode. This means that the surface ionization and the structural ordering of the water layer immediately adjacent to the solid surface due to the surface heterogeneity of β -MnO₂(s) would not significantly reduce the access of Cl⁻ to β-MnO₂ (s) surface, which explains its high CDI efficiency. In the case of δ -MnO₂(s) electrode, the determined resistance and capacitance at the solid-electrolyte interface when no additional bias was applied were similar to that of β-MnO₂ electrode. However, an insulatorlike resistant developing at the diffusion layer was identified, which remained three orders of magnitude greater than that of carbon and β -MnO₂(s) electrode even when bias was applied. This can be realized as highly ionized δ –MnO₂(s) would adsorb counter ions to compensate the surface charge and therefore a dense double layer capacitor was developed that inhibited the accommodation of co-ion in CDI process (Ghaemi et al., 2008). This arrangement later resulted in a high resistance region developing at the diffusion layer that reduced the access of co-ions approaching the surface (Fig. 3e). Accordingly, the low CDI performance of δ –MnO₂ electrode, mainly as a result of reduced Cl⁻ (electro)adsorption, can be realized that the majority of applied bias is wasted by driving Cl⁻ across the resistance at the diffusion layer, not for accommodating them. Based on our EIS results, it is clear that the crucial factor regulating the CDI efficiency would be the degree of ionization of MnO₂(s).

3.4. Structure induced surface charge effect

Above discussions illustrate how ionization of MnO₂(s) surface affects the CDI efficiency. We speculate that the degree of surface ionization is likely regulated by the structure among different MnO₂ phases, specifically the structure induced surface charge effect on the surface heterogeneity. Recently, Ganesan and Murugan employed firstprinciples calculations to explore the water oxidation occurring at α -MnO₂(s) surface (Ganesan and Murugan, 2016). They indicated that an initial step of water oxidation is involved in dissociating water dimers into hydronium intercalated within the network and hydroxide ions accommodated at the oxygen vacant site that strongly interact with Mn atoms in the tunnel of a hydrated α -MnO₂(s) compound. Further, the coulombic attraction of a hydronium ion with a water molecule leads to the formation of a Zundel cation $(H_5O_2^+)$ in the tunnel. Dawson and co-workers conducted another first-principle calculations focusing on oxygen vacancy formation and metallic behavior at a β-MnO₂ grain boundary (Dawson et al., 2015). Their calculations reveal that the formation of oxygen vacancies produces spin-polarized states along with a metallic behavior at the grain boundary with defect charge distributed over a number of oxygen and manganese sites and both of them are important to the electrochemical performance of β-MnO₂. Ghaemi and coworkers experimentally demonstrated that higher specific capacitance of layered δ -MnO₂(s) than that of γ -MnO₂(s) was attributed to the former being capable of physically adsorbing higher amount of water molecules that consequently influenced the proton diffusion process of tunnel structured MnO₂ (Ghaemi et al., 2008). Based on the above experimental results and calculations, it is clear that the structure, particularly the different size of the tunnel structure among the MnO₆ octahedral, strongly influences the electrochemical performance of different phase of MnO₂. Considering that recent first-principle calculations of anatase TiO₂(001) surface suggest that its high surface

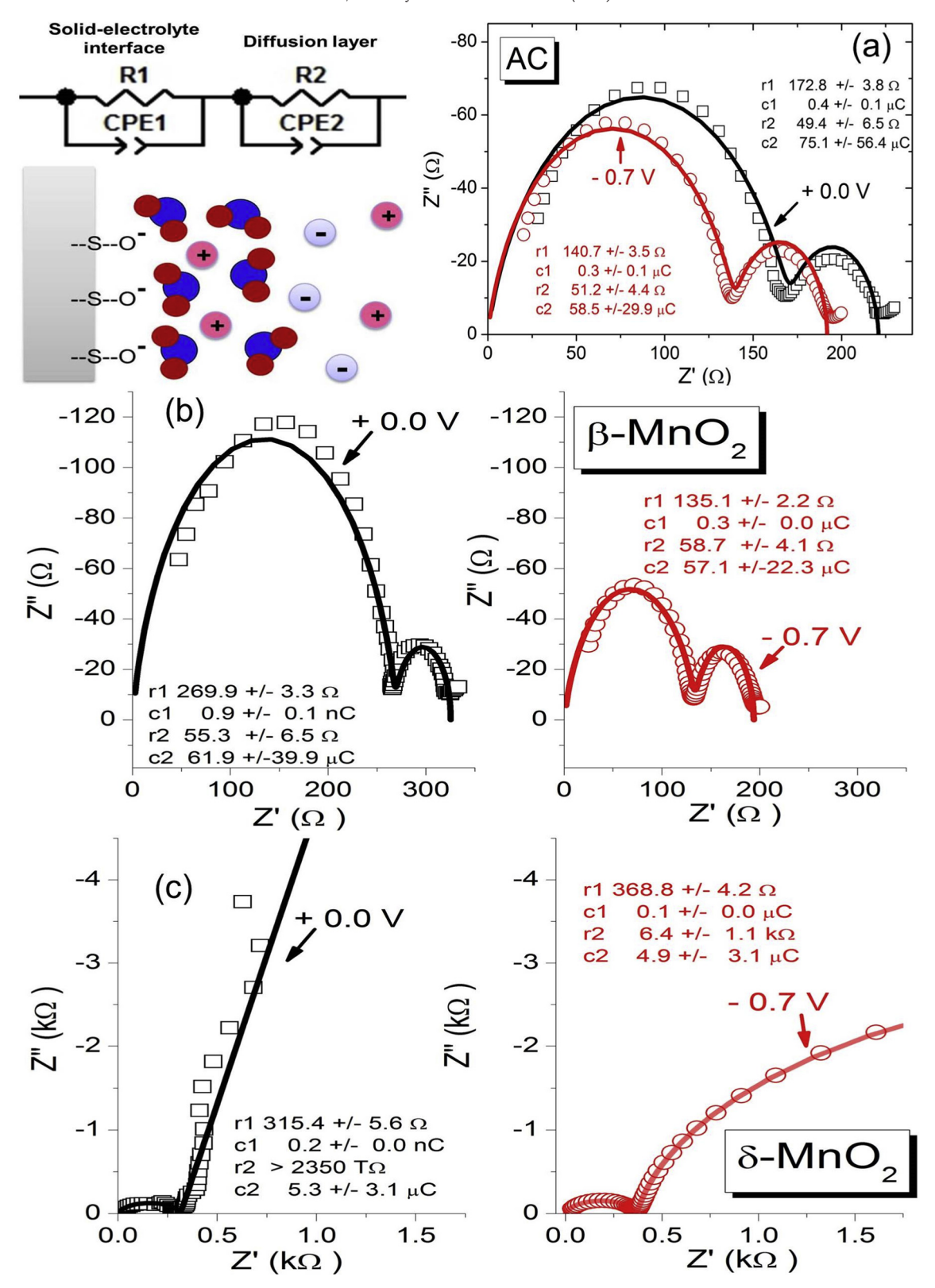


Fig. 5. (a) Illustration of physics background of adopted equivalent circuit (water molecules are presented as two red circles attached on the blue circle, plus and minus signs are referred to cation and anion, respectively) and Nyquist plots and fittings of (a) AC; (b) β -MnO₂; (c) δ -MnO₂ electrodes; black: no bias was applied; red: applied – 0.7 V bias.

reactivity is due to the large surface tensile stress, which can be easily suppressed by a stress-release mechanism (Shi et al., 2017). We further speculate that tensile stress resulting from the tunnel structure among the MnO_6 octahedral is strongly related to the surface heterogeneity

and afterwards reactivity of surface ionization. This surface defect effect might be responsible for the discrepancy in CDI efficiency by different MnO_2 phases, which has never been included and discussed in CDI process previously. Importantly, Shi and co-workers further indicated that

the anatase(001) surface with few defects, which can be achieved by adsorption of water, is important in improving the reactivity (Shi et al., 2017). Consistent with the aforementioned speculation, the structural ordering of the water layer immediately adjacent to the solid surface induced by surface ionization (Huang and Stumm, 1973) would profoundly influence the access of ions moving across the diffusion layer and consequently affect the CDI efficiency. Nonetheless, observed structure induced surface charge effect in this study should be further interpreted at the molecular rather than the mean-field level such as the classical Gouy-Chapman theory and DLVO theory as these theories have limitations in describing certain phenomena at the solidelectrolyte interfaces (i.e., adsorbed ion-ion correlations and hydration forces) (Kobayashi et al., 2017). This information will be the scientific base for designing high efficiency CDI electrodes in the future.

4. Conclusion

In this study, the discrepancy in CDI efficiency brought by different MnO₂ phases was explored by alkalimetric-acidimetric titration and electrochemical impedance spectroscopy analyses. The deionization efficiency decreased with increasing degree of surface ionization of hydrous MnO₂(s), which was independent of the pH and the MnO₂ phases. The structure induced surface charge effect on the surface heterogeneity induced by different phase of MnO₂ played an important role in CDI efficiency. A highly charged surface would induce a high resistance in the diffusion layer that reduces anion (electro)adsorption and consequently compromises CDI efficiency. Furthermore, detailed exploration concerning the adsorbed ion-ion correlations and hydration forces at the solid-electrolyte interfaces at molecular level would be crucial to gain insight into the observed structure induced surface charge and its effect on CDI efficiency.

Acknowledgment

The authors wish to thank the Ministry of Science and Technology. Taiwan, for the support of this study by research grants: MOST 105-2113-M-007-022-MY2 and MOST 106-2113-M-007-014; and by National Science Foundation of Fujian (2018I01526). Addition support was provided by US NSF IOA (1632899).

References

- Abou-Shady, A., 2017. Recycling of polluted wastewater for agriculture purpose using electrodialysis; perspective for large scale application, Chem. Eng. I. 323, 1-18.
- Ahualli, S., Iglesias, G.R., Fernandez, M.M., Jimenez, M.L., Delgado, A.V., 2017. Use of soft electrodes in capacitive deionization of solutions. Environ. Sci. Technol. 51 (9), 5326-5333.
- Albert, M., Clifford, A., Zhitomirsky, I., Rubel, O., 2018. Adsorption of maleic acid monomer on the surface of hydroxyapatite and TiO2: a pathway toward biomaterial composites, ACS Appl. Mater. Interfaces 10 (29), 24382-24391.
- Chen, B.W., Wang, Y.F., Chang, Z., Wang, X.W., Li, M.X., Liu, X., Zhang, L.X., Wu, Y.P., 2016. Enhanced capacitive desalination of MnO2 by forming composite with multi-walled carbon nanotubes. RSC Adv. 6 (8), 6730-6736.
- Chen, C., Xu, K., Ji, X., Miao, L., Jiang, J.J., 2017. Promoted electrochemical performance of beta-MnO₂ through surface engineering. ACS Appl. Mater. Interfaces 9 (17), 15176-15181.
- Choi, I.-A., Kwak, D.-H., Han, S.-B., Park, J.-Y., Park, H.-S., Ma, K.-B., Kim, D.-H., Won, J.-E., Park, K.-W., 2017. Doped porous carbon nanostructures as non-precious metal catalysts prepared by amino acid Glycine for oxygen reduction reaction, Appl. Catal. B. 211 235-244
- Dawson, J.A., Chen, H., Tanaka, I., 2015. First-principles calculations of oxygen vacancy formation and metallic behavior at a β-MnO₂ grain boundary. ACS Appl. Mater. Interfaces 7 (3), 1726-1734.
- El-Deen, A.G., Barakat, N.A.M., Kim, H.Y., 2014. Graphene wrapped MnO₂-nanostructures as effective and stable electrode materials for capacitive deionization desalination technology. Desalination 344, 289–298.
- Fan, C.S., Tseng, S.S., Li, K.C., Hou, C.H., 2016. Electro-removal of arsenic(III) and arsenic (V) from aqueous solutions by capacitive deionization. J. Hazard. Mater. 312, 208-215
- Fazio, G., Selli, D., Ferraro, L., Seifert, G., Di Valentin, C., 2018. Curved TiO₂ nanoparticles in water: short (chemical) and long (physical) range interfacial effects. ACS Appl. Mater. Interfaces 10 (35), 29943-29953.

- Ganesan, K., Murugan, P., 2016. First principles calculations on oxygen vacant hydrated α -MnO₂ for activating water oxidation and its self-healing mechanism. Phys. Chem. Chem. Phys. 18 (32), 22196-22202.
- Gao, X., Omosebi, A., Landon, J., Liu, K.L., 2015. Surface charge enhanced carbon electrodes for stable and efficient capacitive deionization using inverted adsorption-desorption behavior. Energy Environ. Sci. 8 (3), 897-909.
- Gao, X., Porada, S., Omosebi, A., Liu, K.L., Biesheuvel, P.M., Landon, J., 2016. Complementary surface charge for enhanced capacitive deionization. Water Res. 91, 275-282.
- Ghaemi, M., Ataherian, F., Zolfaghari, A., Jafari, S.M., 2008. Charge storage mechanism of sonochemically prepared MnO₂ as supercapacitor electrode: effects of physisorbed water and proton conduction. Electrochim. Acta 53 (14), 4607-4614.
- Huang, C.P., 19 $\hat{7}$ 6. The electrical double layer of γ -Al₂O₃-electrolyte system. In: Kerker, M. (Ed.), Colloid & Interface Science. vol. 4, pp. 29-43.
- Huang, C.P., Stumm, W., 1973. Specific adsorption of cations on hydrous γ-Al₂O₃. J. Colloid
- Interface Sci. 43 (2), 409–420. Huang, Y.L., Cheng, H.H., Shu, D., Zhong, J., Song, X.N., Guo, Z.P., Gao, A.M., Hao, J.N., He, C., Yi, F.Y., 2017. MnO₂-introduced-tunnels strategy for the preparation of nanotunnel inserted hierarchical-porous carbon as electrode material for high-performance supercapacitors supercapacitors. Chem. Eng. J. 320, 634-643.
- Kobayashi, K., Liang, Y.F., Murata, S., Matsuoka, T., Takahashi, S., Nishi, N., Sakka, T., 2017. Ion distribution and hydration structure in the stern layer on muscovite surface. Langmuir, 33 (15), 3892-3899.
- Lado, J.J., Wouters, J.J., Tejedor-Tejedor, M.I., Anderson, M.A., Garcia-Calvoa, E., 2013. Asymmetric capacitive deionization utilizing low surface area carbon electrodes coated with nanoporous thin-films of Al₂O₃ and SiO₂. J. Electrochem. Soc. 160 (8), F71-F78
- Li, L.L., Zhao, R.M., Wang, L., Wu, S.K., Wang, T.H., 2018. Correlation of surface concentration polarization and surface electrochemistry of an asymmetric membrane: an ex situ electrical impedance spectroscopy study. J. Taiwan Inst. Chem. Eng. 82, 367-372.
- Li, P.C., Hu, C.H., Noda, H., Habazaki, H., 2015. Synthesis and characterization of carbon black/manganese oxide air cathodes for zinc-air batteries: effects of the crystalline structure of manganese oxides. J. Power Sources 298, 102-113.
- Linnartz, C.J., Rommerskirchen, A., Wessling, M., Gendel, Y., 2017. Flow-electrode capacitive deionization for double displacement reactions. ACS Sustain. Chem. Eng. 5 (5), 3906-3912.
- Liu, P.I., Chung, L.C., Ho, C.H., Shao, H., Liang, T.M., Chang, M.C., Ma, C.C.M., Horng, R.Y., 2016a. Comparative insight into the capacitive deionization behavior of the activated carbon electrodes by two electrochemical techniques. Desalination 379, 34-41.
- Liu, P.Y., Yan, T.T., Shi, L.Y., Park, H.S., Chen, X.C., Zhao, Z.G., Zhang, D.S., 2017. Graphenebased materials for capacitive deionization. J. Mater. Chem. A 5 (27), 13907–13943.
- Liu, Y.H., Hsi, H.C., Li, K.C., Hou, C.H., 2016b. Electrodeposited manganese dioxide/activated carbon composite as a high-performance electrode material for capacitive deionization. ACS Sustain. Chem. Eng. 4 (9), 4762-4770.
- Macias, C., Rasines, G., Lavela, P., Zafra, M.C., Tirado, J.L., Ania, C.O., 2017. Mn-containing Ndoped monolithic carbon aerogels with enhanced macroporosity as electrodes for capacitive deionization. ACS Sustain. Chem. Eng. 4 (5), 2487-2494.
- Murphy, G.W., Hock, R., Caudle, D., Papastamataki, A., Tucker, J.H., Wood, E.N., Di Luzio, F.C., Gillam, W.S., Johnson, S., 1965. Electrochemical demineralization of water with carbon electrodes. University of Oklahoma; for Office of Saline Water, U.S. Dept. of the Interior, Washington, D.C., p. 188.
- Pan, S.-Y., Snyder, S.W., Lin, Y.-P., Chiang, P.-C., 2018. Electrokinetic desalination of brackish water and associated challenges in the water and energy Nexus. Environ. Sci.: Water Res. Technol. 4, 613-638.
- Prehal, C., Koczwara, C., Jackel, N., Amenitsch, H., Presser, V., Paris, O., 2017. A carbon nanopore model to quantify structure and kinetics of ion electrosorption with in situ small-angle X-ray scattering. Phys. Chem. Chem. Phys. 19 (23),
- Ray, J.R., Wong, W., Jun, Y.-S., 2017. Antiscaling efficacy of CaCO₃ and CaSO₄ on polyethylene glycol (PEG)-modified reverse osmosis membranes in the presence of humic acid: interplay of membrane surface properties and water chemistry. Phys. Chem. Chem. Phys. 19 (7), 5647-5657.
- Shahzad, M.W., Burhan, M., Ang, L., Ng, K.C., 2017. Energy-water-environment nexus underpinning future desalination sustainability. Desalination. 413, 52-64.
- Shao, M.H., Chang, Q.W., Dodelet, J.P., Chenitz, R., 2016. Recent advances in electrocatalysts for oxygen reduction reaction. Chem. Rev. 116 (6), 3594-3657.
- Shi, Y.L., Sun, H.J., Saidi, W.A., Nguyen, M.C., Wang, C.Z., Ho, K.M., Yang, J.L., Zhao, J., 2017. Role of surface stress on the reactivity of Anatase $TiO_2(001)$. J. Phys. Chem. Lett. 8 (8),
- Stumm, W., Morgan, J.J., 1995. Aquatic Chemistry: Chemical Equilibria and Rates in Natural Waters. 3rd edition. Wiley-Interscience Publication.
- Suss, M.E., Porada, S., Sun, X., Biesheuvel, P., M., Yoon, J., Presser, V., 2015. Water desalination via capacitive deionization: what is it and what can we expect from it? Energy Environ. Sci. 8, 2296-2319.
- Wang, T.H., Henderson, C.N., Draskovic, T.I., Mallouk, T.E., 2014. Synthesis, exfoliation, and electronic/protonic conductivity of the Dion-Jacobson phase layer perovskite HLa₂Ti₂TaO₁₀ H₂O. Chem. Mater. 26, 898-906.
- Wang, T.H., Cheng, Y.J., Wu, Y.Y., Lin, C.A., Chiang, C.C., Hsieh, Y.K., Wang, C.F., Huang, C.P., 2016. Enhanced photoelectrochemical water splitting efficiency of hematite electrodes with aqueous metal ions as in situ homogenous surface passivation agents. Phys. Chem. Chem. Phys. 18 (42), 29300–29307.
 Wang, Z., Yan, T.T., Shi, L.Y., Zhang, D.S., 2017b. In situ expanding pores of dodecahedron-
- like carbon frameworks derived from MOFs for enhanced capacitive deionization. ACS Appl. Mater. Interfaces 9 (17), 15068-15078.
- Wang, Z.J., Gong, H., Zhang, Y., Liang, P., Wang, K.J., 2017a. Nitrogen recovery from lowstrength wastewater by combined membrane capacitive deionization (MCDI) and ion exchange (IE) process. Chem. Eng. J. 316, 1-6.

- Xu, X., Liu, Y., Wang, M., Zhu, C., Lu, T., Zhao, R., Pan, L., 2016. Hierarchical hybrids with microporous carbon spheres decorated three-dimensional graphene frameworks for capacitive applications in supercapacitor and deionization. Electrochim. Acta 133, 88–95
- Xu, X.T., Wang, M., Liu, Y., Lu, T., Pan, L.K., 2017. Ultrahigh desalinization performance of asymmetric flow-electrode capacitive deionization device with an improved operation voltage of 1.8 V. ACS Sustain. Chem. Eng. 5 (1), 189–195.
- Yang, J., Zou, L., Song, H.H., Hao, Z.P., 2011. Development of novel MnO₂/nanoporous carbon composite electrodes in capacitive deionization technology. Desalination. 276, 100–206
- Yang, W.J., Zhu, Y.F., You, F., Yan, L., Ma, Y.J., Lu, C.Y., Gao, P.Q., Hao, Q., Li, W.L., 2018. Insights into the surface-defect dependence of molecular oxygen activation over birnessite-type MnO2. Appl. Catal. B 233, 184–193.